PHYSICAL REVIEW B VOLUME 19, NUMBER 3 1 FEBRUARY 1979

# Nuclear resonance of ytterbium local moments in gold

D. Follstaedt and A. Narath
*Sandia Laboratories, Albuquerque, New Mexico 87185*

(Received 24 July 1978)

We have observed the $^{173}$Yb nuclear resonance in dilute *Au*Yb alloys using a phase-coherent spin-echo spectrometer in the frequency range 450–530 MHz, with external fields of 67–119 kOe and temperatures of 1–2 K. At these field strengths and temperatures, the electronic moment is strongly polarized and the local-moment relaxation regime $\omega_e T_2^e >> 1$ applies. The resonance has been studied in both powders and single crystals. The field dependence of the resonance frequencies can be fit with a crystal-field splitting $\Delta(\Gamma_8 - \Gamma_7) = 83.7(\pm 2.5)$ K and a hyperfine constant $A/h = -241.5(\pm 1.0)$ MHz. These values agree well with those obtained in electron-spin-resonance, Mössbauer, and magnetic-susceptibility experiments. The transverse nuclear relaxation time varies as $T_2 \propto T^{-1}$ and $T_2 \propto H_0^2$. The measured rates agree with predictions for the $\frac{1}{2} \leftrightarrow -\frac{1}{2}$ nuclear transition based on a model involving local-moment fluctuations within the $\Gamma_7$ ground-state doublet using a conduction-electron exchange constant $\langle \mathcal{J}^2 \rangle \rho^2 = 0.018$ derived from the reported thermal broadening of the ytterbium ESR. The absence of significant contributions to the observed high-field relaxation rates from $\Gamma_7$-$\Gamma_8$ fluctuations provides strong evidence that the local-moment—conduction-electron interaction in *Au*Yb is principally of an anisotropic form.

## I. INTRODUCTION

Transition and rare-earth impurities which possess magnetic moments describable by a distinct $d$ or $f$ electronic configuration in a nonmagnetic host metal are commonly referred to as "local moments." The properties of such moments are strongly influenced by exchange coupling with host conduction electrons. This interaction is a perturbation on the local-moment eigenstates and causes transitions between them. Theories of local-moment fluctuations identify two regimes distinguished by the inequalities $\omega_e T_2^e << 1$ (high temperature) and $\omega_e T_2^e >> 1$ (low temperature) where $\omega_e$ is the electron-spin resonance frequency of the local moment and $T_2^e$ its inverse linewidth.

Because of the hyperfine coupling between the local moment and its nucleus, the impurity nuclear resonance can be used to probe the local moment.[1] It senses the static magnetization through nuclear resonance frequency shifts, and fluctuations through nuclear relaxation rates. To date, local-moment nuclear relaxation in the high-temperature regime has been studied in the system *Cu* $^{55}$Mn.[2] A lowest-order exchange-perturbation analysis accounts for the $^{55}$Mn relaxation rates with an isotropic-exchange constant which is in good agreement with other experiments. Local-moment nuclear relaxation in the low-temperature regime has been studied in the system *W* $^{59}$Co.[3] In this case, however, the analysis is subject to uncertainties due to higher-order contributions associated with a rather high Kondo temperature ($\Theta_K \sim 2$ K). In order to avoid this complication and thus provide an experimental test of predictions for the low-temperature regime based on perturbation theory, we chose to study the system *Au* $^{173}$Yb.[4] This dilute magnetic alloy has a very low Kondo temperature ($\Theta_K \sim 0.01$ K).[5] Moreover, most of the parameters necessary for interpretation of nuclear-resonance experiments are known from other experiments. Ytterbium dissolves in gold as a trivalent ($J = \frac{7}{2}$) ion. Magnetic-susceptibility measurements by Williams and Hirst[6] and Murani[7] have shown the ground state to be the $\Gamma_7$ doublet, well isolated ($\Delta \sim 90$ K) by crystal-field interactions from the $\Gamma_6$ doublet and $\Gamma_8$ quartet. The $\Gamma_7$ $g$-value and $^{171}$Yb hyperfine coupling constant $A$ ($^{171}$Yb) have been measured in the electron-spin-resonance (ESR) experiments of Tao, *et al.*[8] We report here the detailed results of low-temperature (1–2 K) spin-echo NMR experiments in external magnetic fields of 60–120 kOe. Our experimental conditions were chosen to satisfy $T << \Delta$ and $g_J \mu_B H_0 >> k_B T$ assuring that thermal excitations out of the local-moment ground state were insignificant (i.e., our experiments were restricted to the polarized-moment regime).

Two forms for the exchange interaction have been used to analyze local-moment fluctuations in *Au*Yb. Early ESR[8] and Mössbauer-effect[9–11] (ME) studies assumed the traditional isotropic interaction $-\mathcal{J}\vec{S} \cdot \vec{\sigma}$, where $\vec{S}$ is the local-moment spin and $\vec{\sigma}$ the conduction-electron spin. More recently, an anisotropic-exchange Hamiltonian arising from covalent mixing has been proposed[12,13] which combines the effects of both spin and orbital exchange. In support of this model Gonzales-Jimenez *et al.*[14] argue that for $Yb^{3+}$ impurities, better experimental agreement with ME linewidths is obtained using the anisotropic form. Regardless of which exchange interaction is assumed in deriving the exchange constant for *Au*Yb, essentially identical $^{173}Yb$ nuclear relaxation rates due to fluctuations within $\Gamma_7$ are predicted. The calculated rates are favorable to observation of the resonance in sufficiently strong applied magnetic fields ($T_2 \sim 100$ $\mu$sec for $H_0 \sim 100$ kOe and $T \sim 1$ K). However, significant differences between the two exchange models are predicted at high fields when $\Gamma_8$ contributions to the relaxation are considered. We shall show that our data can distinguish between the two predictions. A major conclusion of our work is that the isotropic-exchange model is inappropriate for *Au*Yb, thus adding to the growing body of knowledge concerning the influence of orbital angular momentum on the electronic properties of dilute magnetic alloys.[12–16]

Because of the rapid exchange-induced fluctuations of the $Yb^{3+}$ moment the rapid relaxation limit $\omega_n T_1^e \ll 1$ applies to our experiments, where $\omega_n$ is the nuclear frequency and $T_1^e$ the electronic spin-lattice relaxation time. Accordingly, a single nuclear resonance shifted by a time-averaged ytterbium hyperfine field is observed as expected, in contrast to the multiple hyperfine transitions previously observed[17] at much lower temperatures in *Au*Er. We chose the isotope $^{173}Yb$ because its resonance frequency ($\sim$500 MHz) was more accessible experimentally than that of $^{171}Yb$ ($\sim$1800 MHz). The very large linewidths encountered and the use of single-crystal samples combined to give very weak signals. The experimental apparatus and techniques dictated by these difficulties are discussed in Sec. II. In Sec. III our observed frequencies as a function of external field strengths are presented. An analysis of these data yields more accurate values for $A$ ($^{173}Yb$) and $\Delta(\Gamma_8\text{-}\Gamma_7)$ than previously available. Evidence for a slight anisotropy in $A$ ($^{173}Yb$) is presented. The inhomogeneous linewidths observed in our experiments are summarized in Sec. IV and possible origins are discussed briefly. The large quadrupole moment of $^{173}Yb$ combined with unavoidably large field- and lattice-strain induced-electric-field gradients at the impurity sites cause complete "wipe out" of the noncentral transitions. This makes reliable measurements of the longitudinal nuclear relaxation time, $T_1$, extremely difficult. We measured instead the transverse relaxation time, $T_2$, and these data are presented in Sec. V. Using lowest-order perturbation theory, we show that the observed field dependence of the relaxation rates cannot be reconciled with an isotropic-exchange model. On the other hand, we demonstrate that an anisotropic-exchange model gives satisfactory agreement with the data. Concluding remarks based on a comparison of our NMR results with previous ESR, ME, and magnetic-susceptibility studies are presented in Sec. VI.

## II. EXPERIMENTAL METHODS

### A. Spin-echo spectrometer

A detailed description of much of our high-frequency spin-echo apparatus has been given before.[18] Our discussion here will emphasize those components and techniques which were added for the *Au*Yb experiments.

To produce the required high-frequency (450–530 MHz) phase-coherent rf pulses, lower-frequency pulses were frequency multiplied at high-power levels using a series of multiplier-amplifier units. In typical experiments the $\sim$25 MHz output of a 2–40 MHz gated, high-power transmitter was successively frequency quintupled, doubled, and doubled again to yield $\sim$500 MHz pulses. The final unit in this chain was a commercial cavity multiplier (Microwave Cavity Labs. Model No. 5025). It can operate either as a doubler or tripler and provides 500 W pulses into a 50 $\Omega$ load in the range 400–1000 MHz. Since the cavity multiplier is easily damaged by reflected power due to any impedance mismatch in the load, the required isolation was provided using the bridge circuit shown in Fig. 1. The three-port circulators A and B (E and M Laboratories) route pulses from the transmitter to the sam-

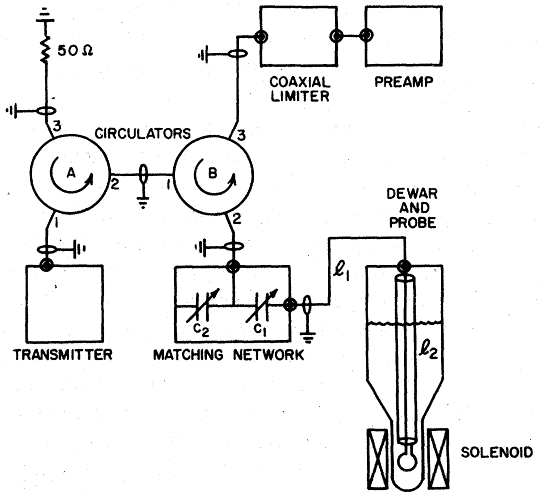

FIG. 1. Schematic diagram of the high-frequency pulsed NMR spectrometer.

ple coil under matched conditions. If a mismatch occurs at the sample-coil port of circulator B, the reflected power is returned to circulator A where it is absorbed at its third port by the 50-$\Omega$ termination. Because of saturation effects in the input circuit of the receiver the impedance seen by the third port of circulator B during the transmitter pulse is effectively zero. This leads to almost total reflection at that port and thus isolates the receiver from the transmitter.

Magnetic fields $H_0 \lesssim 125$ kOe were produced in a $Nb_3Sn$ superconducting solenoid (Intermagnetics Corp.) whose field strength was controlled by use of a copper magnetoresistance sensor. The sample coil was immersed in a pumped liquid-helium bath contained in a separate sample Dewar. A length ($l_2 \approx 4$ ft) of rigid 50-$\Omega$ coaxial cable (Uniform Tubes, Inc.; beryllium-copper conductors, silver-plated inner conductor, and Teflon dielectric) connected the coil with the top of the sample Dewar; a variable length ($l_1 = 6-8$ in.) of flexible coaxial cable connected to the matching network. By varying $l_1$ and the capacitances $C_1$ and $C_2$ (JFD tubular piston capacitors), the effective coil impedance could be matched to the 50-$\Omega$ circulator impedance. The relatively low-power levels used in our experiments (see below) allowed the use of small-diameter teflon-dielectric cables and standard low-voltage tuning capacitors instead of the vacuum-insulated components used in our original version of the spectrometer. Nuclear spin echoes following two equal-width rf pulses appear at the third port of circulator B. A coaxial limiter (Microdynamics Model MD-30L33) protects the low-noise (1–2 dB noise figure) broad-band preamplifier (E and M Laboratories Model CA 2550) from the transmitter overload without significant attenuation of the subsequent echo.

The sample coil geometry was optimized by observing the ferromagnetic nuclear resonance of dysprosium metal[19] in zero external field at 445 MHz. For insulated powdered samples ($\frac{1}{2}$ in. long and $\frac{1}{2}$ in. diameter), a single turn of copper foil of the same dimension was found to be optimum; for $\frac{1}{2}$ in. long $\frac{3}{8}$ in. diameter solid samples, a four-turn coil of $\sim\frac{3}{32}$ in. wide copper foil was found to be best. The *Au*Yb single crystals in such a coil were insulated from the foil by teflon tape. Signal intensities were found to be independent of the thickness of insulating teflon, in agreement with results obtained in low-frequency single-crystal studies.[20] In general, all proton-containing materials were avoided in the vicinity of the solenoid in order to prevent interference from proton resonances.

The ~500 MHz reference needed for phase-sensitive detection was derived from the ~25 MHz master oscillator by use of a Hewlett-Packard Model No. 1D511A spectrum generator, whose 20th harmonic was amplified by a Hewlett-Packard Model 230B tunable amplifier. The phase of this reference was adjusted by a trombone tuner. The remainder of the receiver, consisting of a Communication Electronics, Inc. frequency converter (Type FE-26) and receiver (Type 977) was the same as described earlier.

Repetitive signal averaging was required to achieve adequate detection sensitivity for the very weak $^{173}$Yb echoes. Following two equal-width pulses of time separation $\tau$, a Biomation 610B transient recorder was triggered to digitize the detected and filtered spectrometer output during a time interval centered about the expected echo position. This digitized spectrometer output was transferred to and stored in a Nicolet 1070 signal averager using a Nicolet SD78 interface unit.

The severe inhomogeneous broadening of the $^{173}$Yb resonances in *Au*Yb dictated the use of narrow rf pulses. A minimum pulse width of 3 $\mu$sec was chosen because of transmitter power limitations and the ~1 MHz Biomation bandwidth. (The echo width equals the rf pulse width for our extremely broad resonances.) The rf field $H_1$ in the sample coil was optimized by adjusting the plate-supply voltage of the final transmitter for maximum signal intensity. The approximate rms power levels during the pulses were found to be 400 W for powdered samples and 70 W for the single crystals. These low-power requirements are due to the hyperfine enhancement[21] of the applied $H_1$ by the local moment. Since the electronic relaxation times are much faster than the nuclear frequency ($\omega_n T_1^e \ll 1$), the orientation of the electronic magnetization follows the instantaneous applied field $\vec{H}_0 + \vec{H}_1$ and therefore creates a transverse hyperfine field at the rf frequency of magnitude $H_{1,\mathrm{eff}} \sim H_1 \times (H_{\mathrm{hf}}/H_0)$, where $H_{\mathrm{hf}}$ is the hyperfine field. Since $H_{1,\mathrm{eff}}$ equals approximately $25H_1$ for a polarized local moment in *Au*Yb, one would expect the rf requirements of our experiments to be comparable to proton NMR. The required $H_1$ is actually reduced further by a factor $(I+\frac{1}{2}) = 3$ since we observed only the central transition of an $I=\frac{5}{2}$ nucleus. Experimentally, the optimum $H_1$ was $\sim\frac{1}{2}$ that of protons, in reasonable agreement with predictions.

A series of digital pulse generators [10 MHz clock, transistor-transistor logic (TTL)] was developed to generate the time intervals for our experiments.[22] When operating in the "pulse" or "delay" modes, an input pulse resets the counter to start the time interval. The output is high during the interval, and a short (0.1 $\mu$sec) pulse appears at the end of the interval. In the "clock" mode, the units continually count while putting out a short pulse at the end of each interval and resetting the counter to begin the next interval. With these units the repetition period of the experiment, pulse width, pulse spacing, and timing of the signal digitization could be controlled to within

0.1 $\mu$sec. Repetition rates for the two-pulse sequences were 50 $\text{sec}^{-1}$ for the powders and 200 $\text{sec}^{-1}$ for single crystals. The absence of heating effects at these maximum rates was established by comparing signal intensities with those obtained at slower repetition rates. To obtain adequate signal-to-noise ratios for $T_2$ measurements, as many as $4\times10^5$ echo samplings were frequently needed. With this many repetitions, coherent noise in the form of damped ringing following recovery of the receiver from the transmitter overload was observed up to $\sim$50 $\mu$sec after the second pulse. In order to avoid echo-amplitude errors due to this interference only data for which $\tau \gtrsim 50$ $\mu$sec were regarded significant.

### B. Samples

The powder samples and the first single crystals used in our study were prepared by arc melting appropriate amounts of gold (99.9999%, Cominco American) and $^{173}$Yb (99.9%, isotopically enriched to $\sim$90%, Isotope Sales, Union Carbide, Oak Ridge National Laboratory). Powders were obtained from these alloy ingots by machine milling with a fine tungsten carbide rotary cutter, from which 30 $\mu$m chips were obtained. Single crystals were obtained by remelting the arc-melted ingots in a conical-tip $\frac{3}{8}$ in. diam graphite crucible, which was slowly lowered from the furnace. All samples prepared this way were studied carefully by x-ray diffraction and found to be single crystals with the cylindrical growth axes usually very close to [110] or [100]. Specimens $\frac{1}{2}$ in. long were cut from the central portion by spark erosion and etched lightly in aqua regia.

The arc-melted ingots were subsequently found to be contaminated with copper (0.1–0.5 at.%) which was presumably introduced from the arc-furnace hearth. To examine possible effects of the copper contamination on the NMR data, additional single crystals were grown in the carbon crucible using the pure elemental metals as starting material. The resulting crystal was then inverted, remelted, and grown again. Two such remelts removed the visual evidence of ytterbium segregation. Chemical analysis of a nominal 0.1 at.% crystal grown in this manner indicated ytterbium concentrations of 0.10 at.% at either end of the portion used for the NMR experiments and 0.16 at.% at the top of the ingot. Copper concentrations at these points ranged from 25 to 60 ppm. Other impurities found were trace amounts of Mg, Si, Ag, and Ca. No $3d$ or $4f$ magnetic impurities were detected. For a given ytterbium concentration the integrated resonance intensities were consistently greater in crystals grown from arc-melted starting materials than in crystals grown from mixtures of the elemental metals. Approximately half of the ytterbium in the latter crystals was apparently not detected in the NMR experiments. Arc melting evidently produced better mixing and resulted in greater dispersion of the ytterbium impurities. The only other measurable differences between the two sets of samples were greater NMR linewidths in the arc-melted crystals. These can probably be attributed to the higher concentration of "isolated" ytterbium impurities. Resonance frequencies and relaxation rates, on the other hand, showed no significant differences.

### C. Signal intensities and measurement techniques

An important factor in our ability to observe the $^{173}$Yb signals is the hyperfine enhancement of the nuclear magnetization. Similar to the enhancement of $H_1$, the nuclear magnetization induces a much larger transverse electronic magnetization. The enhancement factor is again given by $H_{\mathrm{hf}}/H_0 \approx 25$.

The best signal-to-noise ratios among the single crystals were obtained with a 0.1 at.% sample which had not been arc melted and was oriented with the external field along [001]. Averaging of $2\times10^5$ repetitive echos gave $S/N \sim 8$ as shown in Fig. 2. The powder signal was comparable in strength, while the signal from the arc-melted 0.1 at.% single crystal was slightly weaker. Concerning the relative sensitivities of powder and single-crystal measurements,[20] dysprosium NMR signals at 445 MHz were nearly ten times stronger from powders than from a $\frac{3}{8}$-in.-diam solid (polycrystalline) specimen. Comparison of $^{173}$Yb integrated signal intensities agrees with this ratio provided account is taken of the reduced single-crystal linewidths.

The determination of resonance positions and transverse relaxation times required the accurate measurement of echo amplitudes as a function of magnetic-field strength and pulse separation, respectively. Due to extreme weakness of the signal, long averaging times were required (up to 8 h for a $T_2$

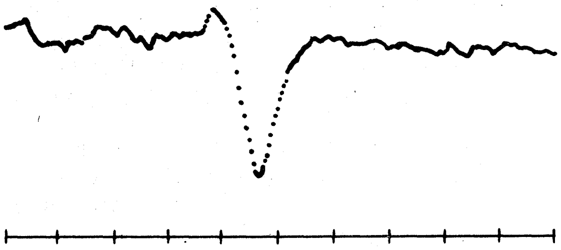

FIG. 2. Signal averager output after accumulating $2\times10^5$ repetitive $Au\ ^{173}\mathrm{Yb}_{0.001}$ spin echoes (copper-free single crystal) at 492 MHz, $\vec{H}_0$ (109.5 kOe) $\parallel$ [001], and 1.1 K. The timing marks indicate 5 $\mu$sec intervals.

measurement), making the results susceptible to drifts in spectrometer sensitivity and other systematic time-dependent errors. This problem was overcome by use of an internal reference. For example, in tracing out a line shape the field strength was alternated at relatively short intervals between a given value and a reference value chosen near the line center. The two sets of echoes were accumulated in separate portions of the signal-averager memory until their intensity ratio was established with sufficient accuracy. Examples of line shapes determined in a point-by-point manner from such ratios are shown in Fig. 3 for two crystal orientations.

In order to apply the ratio method to the $T_2$ measurements, the echo corresponding to the shortest pulse separation ($\tau_0$) was chosen as reference. The timing circuits were programmed to generate a repetitive sequence of four suitably chosen pulse separations ($\tau_0, \tau_1, \tau_2, \tau_3$). The experiment was repeated as necessary for different values of $\tau$, keeping $\tau_0$ fixed, however. The Biomation transient recorder was triggered at appropriate times for each $\tau$ and the data accumulated in corresponding quarters of the Nicolet signal-averager memory. By referring all amplitudes to the $\tau_0$ value the effects of long-term drifts were essentially eliminated. Within our experimental accuracy, all echoes decayed exponentially $[\exp(-2\tau/T_2)]$ and $T_2$ could be determined with an uncertainty ranging from ±6% for the strongest to ±20% for the weakest signals.

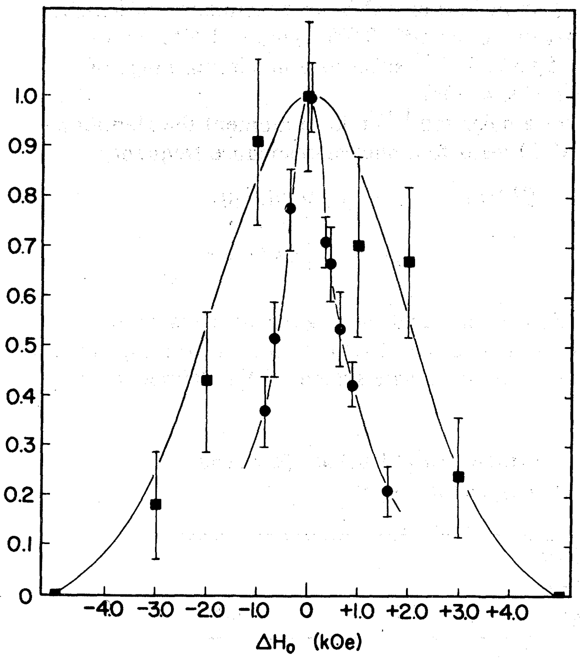

FIG. 3. Plot of normalized experimental $^{173}$Yb spin-echo intensities for a copper-free *Au* $^{173}$Yb$_{0.001}$ single crystal at 500 MHz and 1.1 K. A narrow resonance (●) was obtained with $\vec{H}_0$ (118.5 kOe) ‖ [001] and the broad resonance (■) with $\vec{H}_0$ (95.0 kOe) ‖ [111].

A significant problem encountered in our study was the observation of spurious, nonresonant (i.e., field independent) echoes of unknown origin. These were essentially indistinguishable from "real" spin echoes. Fortunately, in the worst cases these echoes had amplitudes which were only ~20% of the peak signal intensity and necessary corrections were easily applied. Our initial attempts to detect the *Au* $^{173}$Yb resonance involved a tuned re-entrant cavity. However, the spurious signals in this case were unacceptably strong. For this reason the cavity technique was abandoned in favor of the arrangement described above.

## III. RESONANCE FREQUENCIES: EXPERIMENTAL RESULTS AND ANALYSIS

### A. Powdered samples

The first observations of $^{173}$Yb spin echoes were accomplished in 0.1 at.% powdered samples at 1.0 K. At 490 MHz the resonance was centered at 102(4) kOe, with a full width at half-maximum of approximately 25 kOe. It was not possible to determine the frequency dependence of the field for resonance in these samples. At higher frequencies the high-field part of the resonance could not be observed because of the maximum-field limitation of the solenoid ($H_0 \lesssim 125$ kOe). At lower frequencies signal intensities became inadequate because of increasing relaxation rates. Moreover, the variation of $T_2$ with external field strength produced distorted line shapes and hence shifts in the apparent center of the resonance.

The observed linewidths in the powdered samples were somewhat greater than expected. The anisotropy in the ytterbium moment due to field-induced admixture of the $\Gamma_8$ quartet into the groundstate results in a *maximum* calculated field spread at 490 MHz of 21 kOe (see discussion of single-crystal data below). Attempts were made to obtain a narrower powder resonance by annealing, by melting and recrystallization, and by decreasing the ytterbium concentrations to 0.05 at.%. All gave essentially the same ~25 kOe linewidth. Powder studies were consequently abandoned in favor of single-crystal studies.

### B. Single crystals

#### 1. $\vec{H}_0$ ‖ [001]

The resonance data for external fields parallel to the [001] crystal direction are presented in Table I. The most accurate data were obtained with the copper-free 0.1 at.% sample. Comparison of these results with those obtained with other crystals confirms the expected concentration independence of the resonance positions. (The very small but systematic shift to higher fields in the copper-contaminated 0.1 at.% sample might conceivably be attributed to a slight crystal misalignment.)

In general, an analysis of ytterbium hyperfine interactions must consider both magnetic-dipole as well as electric-quadrupole contributions. Although the $\Gamma_7$ ground-state wave functions exhibit cubic symmetry and therefore produce a vanishing electric field gradient (EFG), the field-induced admixture of $\Gamma_8$ into $\Gamma_7$ breaks the symmetry and results in a nonzero quadrupole interaction between the nucleus and $4f$ electrons. Estimates of the interaction for *Au* $^{173}$Yb give

$$\nu_Q \equiv 3e^2qQ[2I(2I-1)h]^{-1} \approx 54 \text{ MHz} \tag{3.1}$$

at 100 kOe, where $Q$ is the nuclear quadrupole moment, and $q$ is the largest principal component of the EFG tensor. In a manifold of constant $J$ it is convenient to express $q$ in terms of the tabulated reduced-matrix element $\alpha$,[23]

$$q = \langle r^{-3} \rangle \langle J \| \alpha \| J \rangle (3\langle m_J^2 \rangle - (\tfrac{63}{4})) \ . \tag{3.2}$$

We have ignored any antishielding effects, and taken $Q = 3.0 \times 10^{-24}$ cm$^2$, $\langle r^{-3} \rangle = 12.5 a_0^{-3}$, and $\langle J \| \alpha \| J \rangle = 0.032$. The field-dependent ground-state eigenfunction was calculated as described below. For $\vec{H}_0 \parallel [001]$ or $[111]$, symmetry requires that the EFG asymmetry parameter be zero, and the orientations of $q$, $\vec{H}_{\text{hf}}$, and $\vec{H}_0$ coincide. The complete nuclear Hamiltonian is then diagonal in the $I^z$ representation. The central transition $(\frac{1}{2} \leftrightarrow -\frac{1}{2})$ is consequently unshifted by the quadrupole interaction regardless of its strength. The noncentral transitions $(m_I \leftrightarrow m_I - 1;\ m_I \neq \frac{1}{2})$ on the other hand, exhibit shifts which, to first order in the quadrupole interaction, are given by $\Delta\nu = \nu_Q(m_I - \frac{1}{2})$. The large magnitude of these calculated shifts supports the conclusion that only the central transition was observed in our experiments.

In the absence of quadrupole perturbations the nuclear resonance frequency $\omega_n$ is governed by the following spin Hamiltonian:

$$\mathcal{H}_n = A_n \vec{I} \cdot \vec{J} - \gamma_n \hbar \vec{I} \cdot \vec{H}_0 (1+K) \ . \tag{3.3}$$

The first term describes the hyperfine coupling between nuclear- and local-moment spins and is the dominant interaction in Eq. (3.3). In the case of Yb$^{3+}$ the orbital motion of the $4f$ electrons provides the principal hyperfine mechanism, contributions from the spin magnetization being relatively unimportant. Within a given $J$ manifold we expect the orbital coupling constant (i.e., $\langle r^{-3} \rangle$) to be essentially independent of the particular eigenfunction, thereby justifying the isotropic form for $H_{\text{hf}}$ in Eq. (3.3). Any anisotropy in the NMR frequency is therefore dominated by anisotropy in the expectation value of $\vec{J}$.

The second term in Eq. (3.3) describes the nuclear Zeeman interaction with the external field

$$[\gamma(^{173}\text{Yb})/2\pi = 0.205 \text{ kHz/Oe}]$$

corrected for any Knight shift ($K$) due to the conduction electrons. The Knight shift can contain contributions which are negative (due to the spin magnetization of $5d$ electrons) as well as positive (due to the orbital magnetization of $5d$ electrons and the spin magnetization of $6s$ electrons). Although we cannot determine either the sign or magnitude of $K$ for the Yb$^{3+}$ impurities in *Au*Yb, an examination of Knight shifts in Yb metal[24] (0.0%), gold (+1.6%), and various $5d$ metals[25–27] suggests a maximum range of $-1\% \leqslant K \leqslant +3\%$.

For a polarized $^{173}$Yb local moment the Hamiltonian (3.3) leads to a nuclear-resonance frequency

$$\omega(^{173}\text{Yb}) = [A(^{173}\text{Yb})/\hbar] \langle 0 | J^Z | 0 \rangle + |\gamma(^{173}\text{Yb})| H_0^Z (1+K) \tag{3.4}$$

where $\omega \equiv 2\pi\nu$, and the angular brackets denote a matrix element computed for the electronic ground state. The coordinate system $X, Y, Z$ defines the

TABLE I. Summary of experimental $^{173}$Yb NMR data in *Au*Yb for $\vec{H}_0 \parallel [001]$ at 1.05 K, and comparison with theory using $\Delta_1 = 83.30$ K, $A/h = -241.47$ MHz, and $K = +1.0\%$.

| $\nu$ (MHz) | $H_0$ (kOe) (calc.) | | $H_0$ (kOe) (obs.) | | |
|---|---|---|---|---|---|
| | | $c$ (at.%) = 0.05 | 0.1 | 0.1[a] | 0.2[a] |
| 362.20 | 0.0 | | | | |
| 450.0 | 66.97 | | 66.98(0.10) | 67.40(0.50) | |
| 475.0 | 91.13 | | 91.23(0.10) | 91.45(0.30) | |
| 492.0 | 109.41 | | 109.41(0.10) | 109.75(0.30) | 109.95(0.60) |
| 500.0 | 118.62 | 118.72(0.10) | 118.51(0.12) | | |

[a]Copper-contaminated samples.

orientation of $\vec{J}$ in the presence of the external field

$$\langle 0|J^X|0\rangle = \langle 0|J^Y|0\rangle = 0 \ , \tag{3.5}$$

$$\langle 0|J^Z|0\rangle = (\langle 0|J^x|0\rangle^2 + \langle 0|J^y|0\rangle^2 + \langle 0|J^z|0\rangle^2)^{1/2} \ . \tag{3.6}$$

The $x,y,z$ coordinates refer to any convenient set of crystallographic axes. In the present case they were chosen to coincide with the [001] direction. For an arbitrary field orientation $\vec{J}$ and $\vec{H}_0$ are not necessarily colinear, of course. However, since $\omega(^{173}\mathrm{Yb})$ is dominated by the hyperfine term any transverse field components of $\vec{H}_0$ have a negligible effect on $\omega_n$ and were therefore neglected in Eq. (3.4). Moreover $H_0^X$ and $H_0^Y$ vanish for symmetry directions such as $\vec{H}_0 \parallel [001]$ or [111].

Both terms in Eq. (3.4) contribute to the observed field dependence of the $^{173}$Yb resonance. The nuclear Zeeman term gives rise to a linear variation with field. The hyperfine term, on the other hand, becomes nonlinear at sufficiently high field strengths because of higher-order field-induced admixture contributions to $\langle 0|J^Z|0\rangle$ arising from the electronic Zeeman term

$$\mathcal{H}_Z = g_J \mu_B \vec{H}_0 \cdot \vec{J} \ , \tag{3.7}$$

where $g_J = \frac{8}{7}$ for Yb$^{3+}$. In other words, the Van Vleck susceptibility becomes field dependent for large $g_J \mu_B H_0/\Delta$. A slight nonlinearity is indeed exhibited by the experimental data in Table I. In order to extract hyperfine and crystal-field parameters from experiment it is necessary to compute $\langle 0|J^Z|0\rangle$ as a function of external field strength, treating the two crystal-field energies $\Delta_1 \equiv \Delta(\Gamma_8 - \Gamma_7)$, $\Delta_2 \equiv (\Gamma_6 - \Gamma_7)$ and the hyperfine constant $A(^{173}\mathrm{Yb})$ as adjustable parameters. This calculation is most conveniently carried out in a crystal-field representation. The $J = \frac{7}{2}$ cubic crystal-field eigenfunctions, which we denote by $|M_i\rangle$ $(i = 0, \ldots, 7)$ are tabulated in Table II in terms of $J^z$ basis functions.[28] Also listed are the eigenvalues of the standard equivalent-operator Hamiltonian

$$\mathcal{H}_{\mathrm{CF}} = B_4(O_4^0 + 5O_4^4) + B_6(O_6^0 - 21O_6^4) \ , \tag{3.8}$$

where $B_4$ and $B_6$ are the fourth- and sixth-order crystal-field parameters, respectively. A $\Gamma_7$ ground state implies $B_4/B_6 \geq \frac{21}{5}$ (i.e., $x \geq 0.20$, in the notation of Lea, Leask, and Wolf[29]). The Zeeman interaction (3.7) for magnetic fields parallel to [001], produces pairwise couplings of the crystal-field levels ($M_0 \leftrightarrow M_3, M_1 \leftrightarrow M_4, M_2 \leftrightarrow M_6, M_5 \leftrightarrow M_7$) and the perturbed eigenfunctions $|M_i\rangle$ and eigenvalues can therefore be expressed in closed form. The latter are plotted in Fig. 4 as a function of the external field. For the ground state we find

$$\langle 0|J^Z|0\rangle = -\tfrac{1}{2} - (8P+1)(16P^2+4P+1)^{-1/2} \ , \tag{3.9}$$

where

$$P \equiv g_J \mu_B H_0/\Delta_1 \ . \tag{3.10}$$

Since the $\Gamma_7$ and $\Gamma_6$ doublets are not coupled for the [001] field orientation the ground-state expectation value of $J^Z$ is independent of the position of $\Gamma_6$. The [001] nuclear-resonance data in Table I therefore yield no information about $\Delta_2$. Using Eq. (3.4) together with Eq. (3.9) a fit to the observed frequencies can be obtained with the parameters listed in Table I. In order to display the relative magnitudes of the various contributions to $\omega(^{173}\mathrm{Yb})$ we consider the 500 MHz resonance. The nuclear Zeeman term contributes 24.6 MHz which is most likely increased by 1% due to the conduction-electron Knight shift ($K$). Pure $\Gamma_7$ states give $\langle 0|J^Z|0\rangle = -\frac{3}{2}$ for Yb$^{3+}$ and hence, in the present case, a zero-field hyperfine frequency of 362.2 MHz, corresponding to a hyperfine field of +1768 kOe. The $\Gamma_8$ admixtures due to the 118.6 kOe external field increases $\langle 0|J^Z|0\rangle$ to $-1.969$ giving rise to the additional 113.2 MHz (i.e., +551 kOe) Van Vleck contribution.

The accuracy with which the model parameters can be determined is limited by the unknown value of $K$. Moreover, in the field range accessible in our experiments variations in $A(^{173}\mathrm{Yb})$ and $\Delta_1$ are not completely distinguishable as regards their effect on the quality of the fit. This is illustrated in Fig. 5 which shows the interrelationship of the three parameters $K$, $A(^{173}\mathrm{Yb})$, and $\Delta_1$. The boxed area indicates ranges of $A(^{173}\mathrm{Yb})$ and $\Delta_1$ for which satisfactory agreement with our data can be obtained, assuming $K$ lies in the range $-1\%$ to $+3\%$. The three dark bands give acceptable values of $A(^{173}\mathrm{Yb})$ and $\Delta_1$ for specific

TABLE II. Cubic crystal-field eigenfunctions $|M_i\rangle$ and eigenvalues $E_i$ for $J = \frac{7}{2}$.

| | $i$ | $\|M_i\rangle$ | $E(M_i) - E(M_0)$ |
|---|---|---|---|
| $\Gamma_7$: | 0 | $(\frac{3}{4})^{1/2}\|-\frac{5}{2}\rangle - (\frac{1}{2})\|+\frac{3}{2}\rangle$ | 0 |
| | 1 | $(\frac{3}{4})^{1/2}\|+\frac{5}{2}\rangle - (\frac{1}{2})\|-\frac{3}{2}\rangle$ | |
| $\Gamma_8$: | 2 | $(\frac{7}{12})^{1/2}\|-\frac{7}{2}\rangle - (\frac{5}{12})^{1/2}\|+\frac{1}{2}\rangle$ | $1200B_4 + 35\,280B_6$ |
| | 3 | $(\frac{1}{2})\|+\frac{5}{2}\rangle + (\frac{3}{4})^{1/2}\|-\frac{3}{2}\rangle$ | |
| | 4 | $(\frac{1}{2})\|-\frac{5}{2}\rangle + (\frac{3}{4})^{1/2}\|+\frac{3}{2}\rangle$ | |
| | 5 | $(\frac{7}{12})^{1/2}\|+\frac{7}{2}\rangle - (\frac{5}{12})^{1/2}\|-\frac{1}{2}\rangle$ | |
| $\Gamma_6$: | 6 | $(\frac{5}{12})^{1/2}\|-\frac{7}{2}\rangle + (\frac{7}{12})^{1/2}\|+\frac{1}{2}\rangle$ | $1920B_4 - 10\,080B_6$ |
| | 7 | $(\frac{5}{12})^{1/2}\|+\frac{7}{2}\rangle + (\frac{7}{12})^{1/2}\|-\frac{1}{2}\rangle$ | |

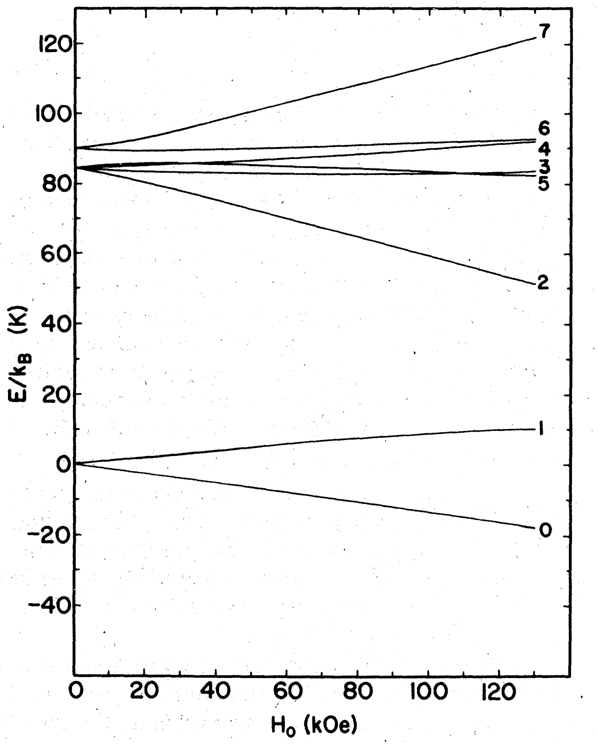

FIG. 4. Field dependence of the $J=\frac{7}{2}$ cubic crystal-field eigenvalues for $\vec{H}_0 \parallel [001]$, assuming $\Delta_1 = 83.3$ K and $\Delta_2 = 90.0$ K. The states are labeled in accordance with the $|M_i\rangle$ states (Table II) from which they are derived.

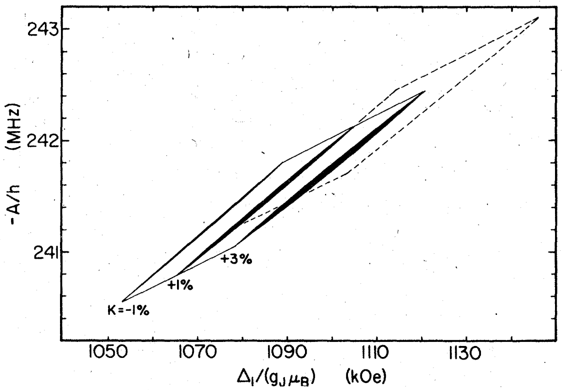

FIG. 5. Relationship between values for $A\,(^{173}\mathrm{Yb})$ and $\Delta_1$ consistent with the [001] resonance data for three assumed Knight shifts. The dashed lines indicate the effect of a 4° crystal misalignment on the parameter fit, as discussed in the text.

values of $K$. These bands are seen to narrow with decreasing $K$; in fact, no fit is possible for $K < -3\%$. We note that any crystal misalignments in our experiments would decrease $\langle 0|J^z|0\rangle$ and consequently result in underestimates of $A\,(^{173}\mathrm{Yb})$ and/or $\Delta_1$. In order to assess the sensitivity of our analysis to such errors the spin Hamiltonian $\mathcal{H}_{\mathrm{CF}} + \mathcal{H}_{\mathrm{Z}}$ was diagonalized using numerical techniques for field orientations corresponding to rotations about the cylindrical axis of the *Au*Yb crystal. (Closed-form solutions are only obtainable for $\vec{H}_0 \parallel [001]$.) The resulting eigenvectors were used to compute $\langle 0|J^z|0\rangle$. The displacement of allowed parameter values for a 4° misalignment is indicated by the dashed lines in Fig. 5. Reproducibility of our data on reinsertion of single-crystal specimens into the NMR probe suggests that alignment errors in the 0.1-at.% (copper-free) experiments did not exceed 2°. Since the variation in the derived parameter depends quadratically on misalignment this source of error therefore appears to be relatively unimportant. Nevertheless, in order to achieve maximum internal consistency in calculating the [001] error bounds in Fig. 5 we restricted ourselves to the 450 , 475 , and 492 MHz data since these were obtained without disturbing the crystal alignment. The 500 MHz measurement followed removal of the crystal from the probe and served as a final check.

### 2. $\vec{H}_0 \parallel [111]$

The data obtained with $\vec{H}_0 \parallel [111]$, Table III, are less accurate than the [001] data because of broader lines and weaker intensities. For this reason experiments with a 0.1 at.% copper-free crystal were carried out at only one frequency. A comparison of the [001] and [111] data reveals a large anisotropy of the NMR frequency. At a constant field strength these two orientations represent extrema with respect to $\langle 0|J^z|0\rangle$. Admixture effects are strongest for $\vec{H}_0 \parallel [111]$, giving $\langle 0|J^z|0\rangle = -2.10$ at 115 kOe, which compares with $\langle 0|J^z|0\rangle = -1.96$ for the [001] orientation.

TABLE III. Summary of experimental $^{173}$Yb NMR data in *Au*Yb for $\vec{H}_0 \parallel [111]$ at 1.05 K, and comparison with theory using $\Delta_1 = 83.30$ K, $\Delta_2 = 90.0$ K, $A/h = -240.1$ MHz and $K = +1.0\%$.

| $\nu$ (MHz) | $H_0$ (kOe) (calc) | $H_0$ (kOe) (obs.) | |
|---|---|---|---|
| | | $c$(at.%) = 0.1 | 0.1[a] |
| 360.15 | 0.0 | | |
| 470.00 | 73.67 | | 74.0(1.5) |
| 485.00 | 84.12 | | 84.0(1.5) |
| 500.00 | 94.71 | 95.0(0.5) | 94.0(1.5) |
| 515.00 | 105.46 | | 105.0(1.5) |
| 530.00 | 116.37 | | 114.5(2.0) |

[a] Copper-contaminated sample.

In fitting the model parameters to the [111] data we initially chose $\Delta_2 = 90$ K as suggested by the temperature dependence of the magnetic susceptibility.[6] Because of our relatively large experimental uncertainties it was found that agreement with the data was possible over a considerable range of parameter values. This is demonstrated in Fig. 6 for $K = +1\%$ and a range of $\Delta_1$ values consistent with the [001] fit, which is shown for comparison. It is apparent that there exists no common solution for the two orientations. Two explanations suggest themselves: (i) The calculated magnitude of $\langle 0|J^Z|0\rangle$ is too large because of an incorrect estimate for $\Delta_2$. (ii) The hyperfine constant is smaller for $\vec{H}_0 \parallel [111]$ than for $\vec{H}_0 \parallel [001]$ (i.e., $A$ is anisotropic). As shown in Fig. 6, however, the disparity is not removed even if maximum values are assumed for $\Delta_2$ ($\Delta_2 = \frac{8}{5}\Delta_1; x = 1$). The dependence of $\langle 0|J^Z|0\rangle$ on $\Delta_2$ is exhibited explicitly in Fig. 7, assuming $\Delta_1 = 83.3$ K. The relative insensitivity over the entire range of $\Delta_2$ values consistent with a $\Gamma_7$ ground state ($0 < \Delta_2 \leq \frac{8}{5}\Delta_1$; $0.2 < x \leq 1$) is a consequence of the fact that neither $J^Z$ nor $J^{\pm}$ have nonvanishing matrix elements directly connecting the $\Gamma_7$ and $\Gamma_6$ levels. We are forced to conclude that the hyperfine constant in Eq. (3.3) is anisotropic. The magnitude of the anisotropy can unfortunately not be determined unambiguously from our results since $\Delta_1$, $\Delta_2$, and $K$ are not known independently. For illustrative purposes we may assume $\Delta_1 = 83.3$ K, $\Delta_2 = 90$ K, $K = +1\%$ and obtain $\Delta A/A = 0.0054$. Such small anisotropy could conceivably arise from higher-order contributions of the hyperfine interaction[30] [e.g., terms of the form $I^Z(J^Z)^3$]. Among mechanisms leading to an intrinsic anisotropy in $A$ are a possible orientation dependence of the local conduction-electron spin-polarization contribution to the ytterbium hyperfine field (i.e., anisotropic local-moment–conduction-electron exchange), or an explicit

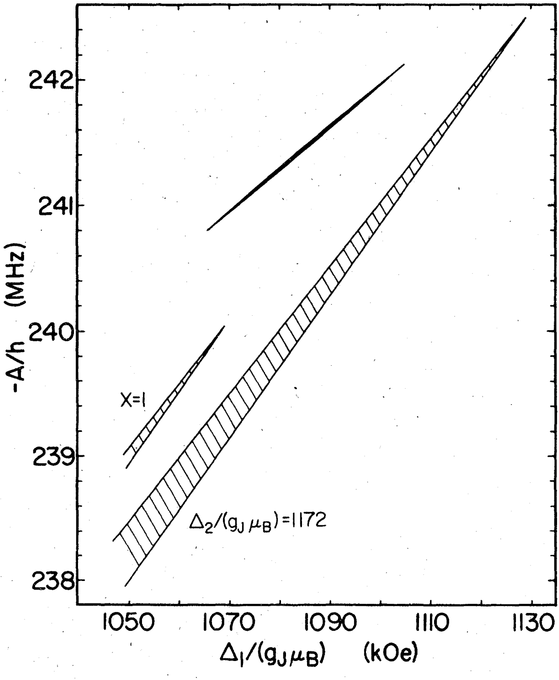

FIG. 6. Relationship between values for $A$ ($^{173}$Yb) and $\Delta_1$ consistent with the [111] resonance data, assuming $K = +1.0\%$. The two cross-hatched regions correspond to different assumed values for $\Delta_2$ (see text). For comparison, the solid band is shown representing the $K = +1.0\%$ fit for the [001] field orientation.

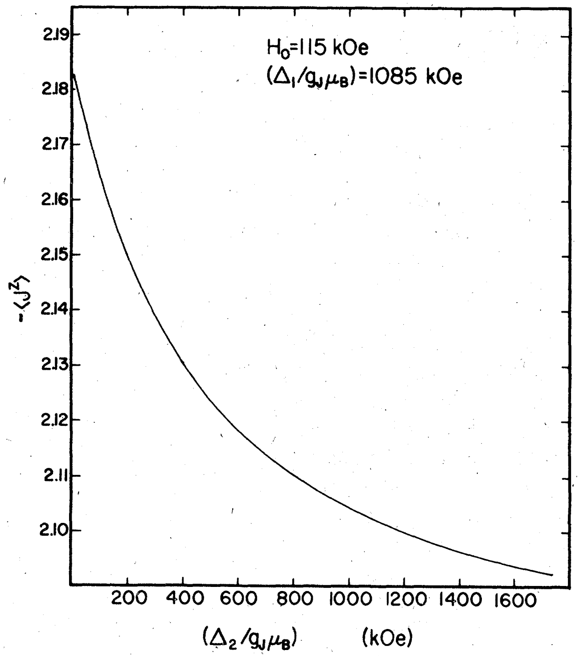

FIG. 7. Variation of $\langle J^Z\rangle$ with $\Delta_2$. The calculation assumes $\Delta_1 = 83.3$ K and $\vec{H}_0(115 \text{ kOe}) \parallel [111]$.

TABLE IV. $^{173}$Yb resonance widths.

| Sample (at.%) | Orientation | Applied field (kOe) | Width (kOe) |
|---|---|---|---|
| 0.05 | [001] | 119 | 1.1(0.2)[b] |
| 0.1 | [001] | 67–118 | 0.7–1.4[b] |
|  | [111] | 95 | 4.0(0.5) |
| 0.1[a] | [001] | 67–110 | 3.5(0.5) |
|  | [111] | 75–115 | 12.0(1.0) |
| 0.2[a] | [001] | 110 | 7.0(1.0) |
| 0.05<br>0.1 | Powder | 102 | ~25 |

[a] Copper contaminated.

[b] See Fig. 8.

dependence of the $4f$ radial wave functions on the particular crystal-field level, leading to small differences between the $\Gamma_7$, $\Gamma_6$, and $\Gamma_8$ oribital hyperfine fields.

## IV. RESONANCE WIDTHS

The linewidth data (full width at half-maximum) for $T \approx 1$ K are summarized in Table IV. We begin the discussion of possible broadening mechanisms by examining the narrowest lines first.

The widths for the copper-free 0.1 and 0.05 at.% samples obtained with $\vec{H}_0 \parallel [001]$ are plotted in Fig. 8. The line through the data suggests a linear field dependence, although a residual linewidth at zero field cannot be ruled out. A likely explanation for this field dependence, which does not appear to be strongly concentration dependent, is a variation in $\Delta_1$ values at different Yb sites. This could result from lattice strains (which occur easily in gold) and would lead to a distribution of hyperfine fields. If so, our measurements suggest a $\Delta_1$ variation of approximately $\pm 0.5\%$ in $\Delta_1$. The fact that the high-field linewidths for the two copper-free compositions are essentially identical suggests that broadening due to the ytterbium impurities is relatively unimportant at these low concentrations. In this connection we note that the arc-melted alloys exhibit significantly greater linewidths, which are field independent but concentration dependent. With $\vec{H}_0 \parallel [001]$ the observed widths are 3.5(0.5) and 7(1) kOe for the 0.1 and 0.2 at.% samples, respectively. Sources of field-independent broadening include Ruderman-Kittel-Kasuya-Yosida (RKKY) and dipolar fields of nearby Yb impurities, which would be field independent since the moments are always polarized in our experiments. The arc-melted samples have a different linewidth than the copper-free sample presumably because of a higher dissolved Yb concentration.

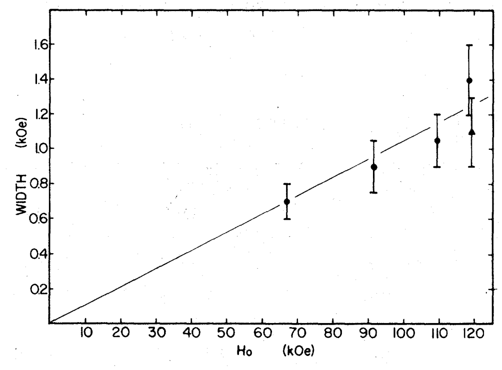

FIG. 8. Plot of $^{173}$Yb spin-echo linewidths (full width at half-maximum) as a function of applied field strength at 1.1 K and $\vec{H}_0 \parallel [001]$ for copper-free samples. The triangle and circles refer to ytterbium concentrations of 0.05 and 0.1 at.%, respectively. The solid line represents a linear fit to the data.

The most puzzling feature of the linewidths is the extreme angular dependence. When the arc-melted 0.1 at.% sample is oriented with $\vec{H}_0 \parallel [111]$ the field-independent linewidth becomes 12(1) kOe. It decreases to 4.0(0.5) kOe in the copper-free sample at 95.0 kOe, but is still anisotropic as shown in Fig. 3. We are unable to offer an explanation for the observed anisotropy.

## V. TRANSVERSE RELAXATION TIMES

### A. Experimental results and general remarks

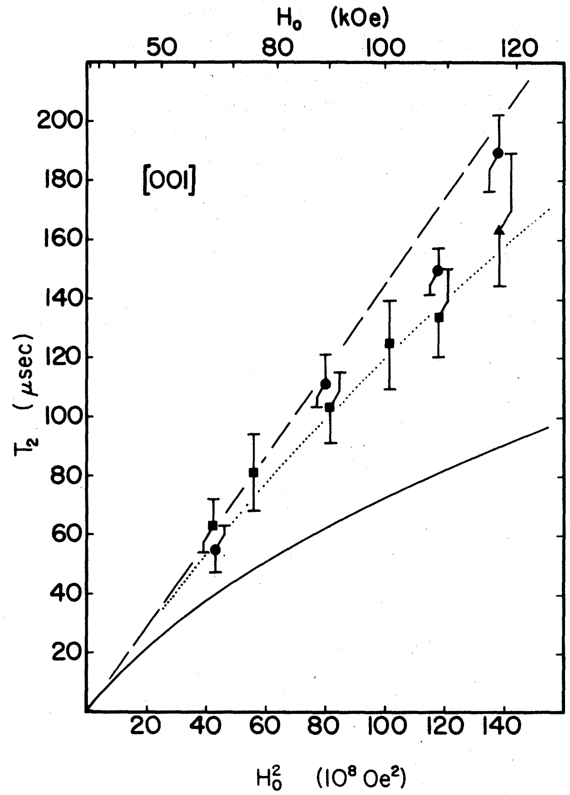

FIG. 9. Field dependence of $T_2$ in $Au\,^{173}$Yb single crystals at 1.05 K with $\vec{H}_0 \parallel [001]$. The triangle (▲) and circles (●) refer to copper-free crystals with respective ytterbium concentrations of 0.05 and 0.1 at.%; the squares (■) refer to a copper-contaminated 0.1 at.% crystal. The lines represent theoretical calculations for the isotropic exchange model as discussed in the text. Dashed line: contribution from pure $\Gamma_7$ level; dotted line: $\Gamma_7$ contribution including field-induced admixture effects; solid line: complete theory, including effects from virtual transitions to excited crystal-field levels.

The most accurate relaxation rates were obtained with the 0.1 and 0.05 at.% copper-free *Au*Yb single crystals and a [001] field orientation. These $T_2$ data are plotted versus $H^2$ in Fig. 9 for $T = 1.05$ K. Also shown for comparison are [001] data for a 0.1 at.% arc-melted single crystal; measurements on this latter sample with a [111] field orientation gave results, Fig. 10, which were essentially identical. The data suggest that $T_2$ may be slightly longer at high fields for [111] than [001]. In view of the experimental uncertainties such conclusion must be regarded as speculative, however. Finally, relaxation experiments were performed on a 0.2% arc-melted single crystal in a [001] orientation, again yielding essentially identical results. Exponential spin-echo decays were observed in every case. (The uncertainties for the arc-melted crystals are generally somewhat greater than for the copper-free crystals because of the smaller echo amplitudes.) We conclude that the transverse nuclear-spin relaxation in *Au* $^{173}$Yb is insensitive to sample-preparation technique and essentially independent of field orientation. The temperature dependence was examined in the range 1.05–2.0 K. (Accurate measurements at higher temperatures were precluded by signal-to-noise considerations.) As shown in Fig. 11, the observed rates are consistent with a constant value for $T_2T$.

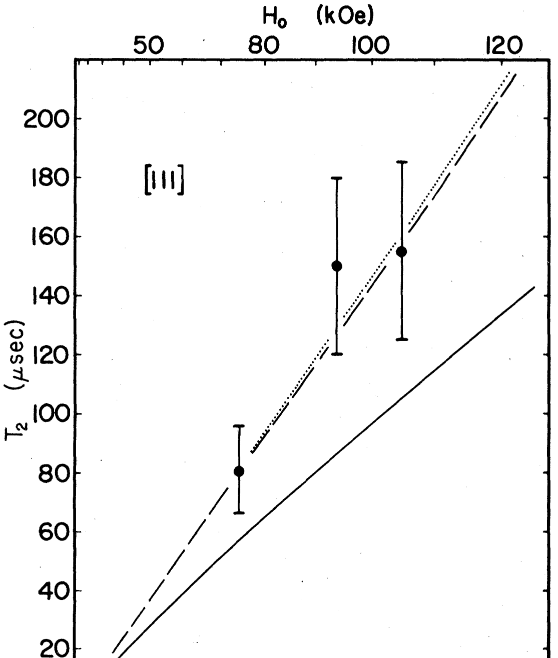

FIG. 10. Field dependence of $T_2$ in a 0.1 at.% copper-contaminated single crystal of *Au* $^{173}$Yb at 1.05 K with $\vec{H}_0 \parallel [111]$. The notation for the theoretical curves is identical to that in Fig. 9.

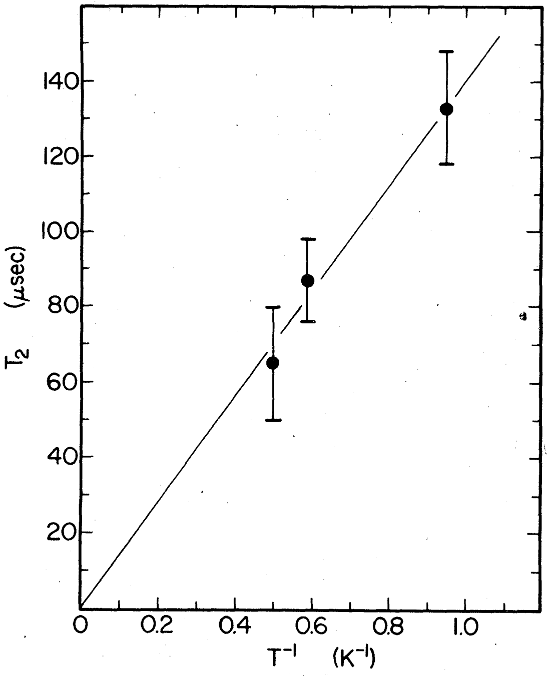

FIG. 11. Temperature dependence of $T_2$ in a copper-contaminated 0.1 at.% *Au* $^{173}$Yb single crystal at 492 MHz with $\vec{H}_0$(109.8 kOe) $\parallel$ [001].

The measured relaxation rates are seen to be quite rapid. We have considered relaxation due to direct hyperfine coupling with *s*- or *d*-like conduction electrons as a possible mechanism. However, comparison with nuclear spin-lattice relaxation rates in 5*d* metals[25,26,31] shows that this mechanism is too weak by several orders of magnitude. We may therefore assume that the *Au* $^{173}$Yb rates are determined by local-moment fluctuations.

The transverse nuclear relaxation rate can be expressed as

$$T_2^{-1} = T_{\parallel}^{-1} + \eta_{\perp} T_{\perp}^{-1} \ , \tag{5.1}$$

where $T_{\parallel}^{-1}$ and $T_{\perp}^{-1}$ are contributions from longitudinal and transverse fluctuations of the hyperfine field, respectively.[32,33] The transverse term is enhanced by a factor $\eta_{\perp}$ in cases where spin diffusion among the $2I$ nuclear transitions is inhibited by inhomogeneous broadening. For the $m_I \leftrightarrow m_I - 1$ transition we find (for odd $I$)

$$\eta_{\perp}(m_I \leftrightarrow m_I - 1) = 2I(I+1) - 2m_I(m_I - 1) - 1 \ . \tag{5.2}$$

In the case of *Au*Yb we have argued above that only the $+\frac{1}{2} \leftrightarrow -\frac{1}{2}$ transition is observed because of strain and field-induced electric quadrupole "wipe-out" effects. Thus $\eta_{\perp} = 17$.

In the low-temperature regime, longitudinal fluctuations vanish for a polarized moment according to[34]

$$T_{\parallel}^{-1} \propto \exp(-g\mu_B H_0/k_B T) \quad . \tag{5.3}$$

This rapid dependence on $H_0/T$ is absent in Figs. 9 and 10. Moreover, calculations based on the theoretical models discussed below yield negligible estimates for $T_{\parallel}^{-1}$ at our field strengths and temperatures. Thus, we arrive at the conclusion that the observed rates are due entirely to transverse fluctuations, $T_2^{-1} = \eta_\perp T_\perp^{-1}$.

It has been shown[34] that for a polarized moment $T_\perp^{-1}$ is determined by virtual excitations of the local moment under the combined influence of the exchange and hyperfine interactions.

$$T_\perp^{-1} = \frac{2\pi}{\hbar} \sum_{i,f} |\mathcal{H}_{if}^{(2)}|^2 \delta(E_i - E_f) \quad , \tag{5.4}$$

where $\mathcal{H}_{if}^{(2)}$ is the second-order matrix element

$$\mathcal{H}_{if}^{(2)} = \sum_m \frac{\langle f | \mathcal{H}_{\mathrm{ex}} + \mathcal{H}_{\mathrm{hf}} | m \rangle \langle m | \mathcal{H}_{\mathrm{ex}} + \mathcal{H}_{\mathrm{hf}} | i \rangle}{E_i - E_m} \quad . \tag{5.5}$$

Here $\mathcal{H}_{\mathrm{ex}}$ and $\mathcal{H}_{\mathrm{hf}}$ are the conduction-electron exchange interaction and hyperfine interaction, respectively, and $|i\rangle$ and $|f\rangle$ specify initial and final states of the combined nuclear–local-moment–conduction-electron system. In order to simplify the notation we have made the usual implicit assumption that $I = \frac{1}{2}$ and the initial and final nuclear spin states in (5.4) are therefore $m_I = +\frac{1}{2}$ and $-\frac{1}{2}$, respectively. The results, of course, are quite general (i.e., independent of $I$). The intermediate states, $|m\rangle$, correspond to virtual transitions of the local moment from its ground state. For the special case of a completely polarized Yb$^{3+}$ local moment the sum over $|m\rangle$ spans the excited states of the $J = \frac{7}{2}$ manifold in the presence of crystal-field and Zeeman interactions. Because of the $\Delta m_J = \pm 1$ selection rules for the angular-momentum matrix elements in Eq. (5.5) only a single intermediate state would contribute for a given $|i\rangle$ and $|f\rangle$ in the absence of crystal-field splittings. The possibility of multiple virtual transitions is a direct consequence of the fact that the crystal-field eigenstates $|J,M\rangle$ are linear combinations of the $|J,m_J\rangle$ free-ion states. It is this feature that distinguishes the present treatment from earlier discussions[34,35] of local-moment nuclear relaxation.

### B. Isotropic exchange model

We now compute $T_2^{-1}$ for the case of an isotropic local-moment–conduction-electron interaction:

$$\mathcal{H}_{\mathrm{ex}}^{(\mathrm{iso})} = -\mathcal{J}(g_J - 1)\vec{\mathrm{J}} \cdot \sum_{\vec{\mathrm{k}},\vec{\mathrm{k}}'} \sum_{\sigma,\sigma'} C_{\vec{\mathrm{k}}',\sigma'}^{\dagger} \vec{\sigma} C_{\vec{\mathrm{k}}\sigma} \quad . \tag{5.6}$$

Here the local-moment spin ($\vec{\mathrm{S}}$) has been projected on the total angular momentum ($\vec{\mathrm{J}}$) in the usual manner

$$\vec{\mathrm{S}} = (g_J - 1)\vec{\mathrm{J}} \quad . \tag{5.7}$$

As in Sec. III, the external-field orientation defines the axis of quantization for the angular momenta (e.g., $J^{\pm} = J^X \pm iJ^Y$). The conduction-electron creation-annihilation operators ($C^{\dagger}/C$) have been defined in a plane-wave representation $|\vec{\mathrm{k}}, \sigma\rangle$. Denoting the $2J+1$ local-moment crystal-field + Zeeman eigenstates by $|\mathcal{M}\rangle$, the states in Eq. (5.4) may be specified in the following way: $|i\rangle = |+\frac{1}{2}, \mathcal{M}_0, \vec{\mathrm{k}}, -\frac{1}{2}\rangle$; $|f\rangle = |-\frac{1}{2}, \mathcal{M}_0, \vec{\mathrm{k}}', +\frac{1}{2}\rangle$; and $|m\rangle = |-\frac{1}{2}, \mathcal{M}_m, \vec{\mathrm{k}}, -\frac{1}{2}\rangle$ or $|+\frac{1}{2}, \mathcal{M}_m, \vec{\mathrm{k}}', +\frac{1}{2}\rangle$, depending on whether the local-moment ground state $|\mathcal{M}_0\rangle$ is connected with a given excited state $|\mathcal{M}_m\rangle$ by the operator $J^+$ or $J^-$ in $(\mathcal{H}_{\mathrm{ex}} + \mathcal{H}_{\mathrm{hf}})$, respectively.

An important feature of the isotropic form (5.6) of the local-moment–conduction-electron interaction is the fact that $\vec{\mathrm{k}}$ and $\sigma$ are independent of $\mathcal{M}$, and determined entirely by overall energy conservation requirements in Eq. (5.4),

$$E_{\vec{\mathrm{k}},\sigma'} - E_{\vec{\mathrm{k}},\sigma} = \hbar\omega_n \quad . \tag{5.8}$$

The summations over $|i\rangle$ and $|f\rangle$ in Eq. (5.4) may therefore be carried out separately from that over $|m\rangle$ in Eq. (5.5) yielding

$$T_\perp^{-1} = \frac{1}{8}\left(\frac{\pi}{\hbar}\right) A^2 (g_J - 1)^2 \langle \mathcal{J}^2 \rangle \rho^2 k_B T \times \left( \sum_{m \neq 0} \left( |\langle \mathcal{M}_m | J^+ | \mathcal{M}_0 \rangle|^2 + |\langle \mathcal{M}_m | J^- | \mathcal{M}_0 \rangle|^2 \right) \times [E(\mathcal{M}_m) - E(\mathcal{M}_0)]^{-1} \right)^2 \quad , \tag{5.9}$$

where $\langle \mathcal{J}^2 \rangle$ indicates an average of $\mathcal{J}^2$ over the Fermi surface, and $\rho$ is the conduction-electron density of states for one spin direction at the Fermi energy. It is evident that contributions from different intermediate states add coherently [i.e., the terms within the large parentheses in Eq. (5.9) are summed before squaring]. As a consequence of this interference, excited crystal-field levels make a fractional contribution to $T_2^{-1}$ of order $H/\Delta$, rather than $(H/\Delta)^2$ if the terms added incoherently.

#### 1. $\vec{\mathrm{H}}_0 \parallel [001]$

When $\vec{\mathrm{H}}_0 \parallel [001]$, $J^+$ and $J^-$ connect the $\Gamma_7$ ground state with the other $\Gamma_7$ level ($\mathcal{M}_1$), two of the $\Gamma_8$ levels ($\mathcal{M}_2, \mathcal{M}_3$), and one $\Gamma_6$ level ($\mathcal{M}_6$). The $\Gamma_6$ coupling vanishes in zero field, and this level therefore contributes only because of field-induced admixture. Using Eq. (5.9) we have computed $T_2^{-1}$ ($=17T_\perp^{-1}$) as a function of field strength, treating admixture effects on the matrix elements and energies numerically as before. Choosing $\Delta_1 = 83.3$ K, $\Delta_2 = 90$ K, and $A/h = 241.5$ MHz (i.e., $A = 160.0 \times 10^{-20}$ ergs) from our frequency analysis (Sec. III), and $\langle \mathcal{J}^2 \rangle \rho^2 = 0.018$ from ESR and ME broadening measurements, yields the solid curve in Fig. 9. For field strengths relevant to the present discussion the $\Gamma_6$ contribution to the low-frequency fluctuation amplitude is small; the rates are for practical purposes insensitive to the precise position of the $\Gamma_6$ level (e.g., at 100 kOe the $\Gamma_6$ contribution is only 5.3% of the calculated rate in Fig. 9). It is apparent that the theory underestimates the relaxation time, the relative disagreement becoming greater with increasing field strength. The disparity is too large to be attributed to uncertainties in the model parameters. For example, it would require at least a 33% *decrease* in $\langle \mathcal{J}^2 \rangle \rho^2$ to account for our high-field data. This corresponds to approximately twice the uncertainty in the ESR thermal-broadening data ($\langle \mathcal{J}^2 \rangle \rho^2 = 0.017 \pm 0.003$). The fact that the various analyses of the ME spectral broadening suggest a slightly *larger* value ($\langle \mathcal{J}^2 \rangle \rho^2 = 0.019$) than used here also argues against this explanation. Finally, we note that the experimental relaxation times are essentially proportional to $H_0^2$ in contrast to the strong curvature in this representation predicted by the theory.

It is instructive to exhibit explicitly the contribution from the $\Gamma_7$-$\Gamma_8$ fluctuations to the calculated rates in Fig. 9. Neglecting the $\Gamma_8$ level (i.e., letting $\Delta_1, \Delta_2 \rightarrow \infty$) reduces Eq. (5.9) to the expression

$$T_1^{-1} = (9\pi/8\hbar) A^2 (g_J - 1)^2 \langle \mathcal{J}^2 \rangle \rho^2 (g_J \mu_B H_0)^{-2} k_B T \quad , \tag{5.10}$$

and yields the dashed line in Fig. 9. Including the field-induced admixture of the $\Gamma_8$ and $\Gamma_7$ levels in the calculation of the $\Gamma_7$ transition matrix element $\mathcal{H}_{if}^{(2)}$ produces a slight increase in the calculated high-field rates, as shown by the dotted curve in Fig. 9. Because of the excellent agreement between experiment and the $\Gamma_7$-only theory we may conclude that the principal shortcoming of the isotropic exchange model lies in its overestimate of contributions from $\Gamma_7$-$\Gamma_8$ virtual transitions.

In the foregoing discussion we ignored the $g$ shift due to conduction-electron exchange which, in principle, affects all of the Zeeman energies in the problem. This correction is relatively unimportant, however, as can be verified by noting that the shift is given, approximately by[36]

$$\Delta g/g = [(g_J - 1)/g_J] \langle \mathcal{J} \rangle \rho \quad . \tag{5.11}$$

Assuming $\langle \mathcal{J} \rangle \rho = -\langle \mathcal{J}^2 \rangle^{1/2} \rho = -0.134$ yields $\Delta g/g = 0.017$, corresponding to a ~3% increase in the nuclear relaxation rate Eq. (5.10).

### 2. $\vec{H}_0 \parallel [111]$

For this field orientation $J^+$ and $J^-$ connect the $\Gamma_7$ ground state with all of the excited levels because of extensive admixture effects. Nevertheless, the $\Gamma_7$-$\Gamma_8$ and $\Gamma_7$-$\Gamma_6$ fluctuations are less effective in contributing to nuclear relaxation in this orientation than [001]. The results of a numerical calculation based on the exact eigenstates are shown in Fig. 10. (We have chosen the same parameters as in the [001] calculations, ignoring the anisotropy in $A$ because of its small magnitude.) The influence of admixture on the $\Gamma_7$-only rate has the opposite sign to that exhibited by the [001] rates; its magnitude, however, is very small, and the two $\Gamma_7$ relaxation rates (i.e., with and without admixture) are consequently difficult to distinguish on the scale of Fig. 10. It is interesting to note that whereas $\langle J^z \rangle$, and hence the static hyperfine field, are largest for $\vec{H}_0 \parallel [111]$, the calculated relaxation rate appears to be a minimum in this orientation.

As in the case of the [001] data a comparison of theory and experiment for $\vec{H}_0 \parallel [111]$, Fig. 10, strongly favors the $\Gamma_7$-only theory. Because of the larger experimental uncertainty for the [111] orientation this conclusion is, of course, less definitive. We also note that contributions from $\Gamma_7$-$\Gamma_8$ virtual transitions and/or $\Gamma_8$ admixtures into the $\Gamma_7$ levels lead to appreciable anisotropy, the calculated high-field relaxation times being longer for the [111] orientation than [001]. This effect is in agreement with trends suggested by the experimental observations.

### C. Anisotropic exchange model

We now demonstrate that the ineffectiveness of the excited crystal-field levels in contributing to local-moment nuclear relaxation in *Au*Yb is a consequence of the orbital degeneracy of the $Yb^{3+}$ ion. This degeneracy leads to orbital exchange scattering and hence an anisotropic form for the local-moment–conduction-electron exchange interaction, as discussed, for example, by Coqblin and Schrieffer.[12] These authors treated the case of dominant covalent-mixing exchange in the limit of *jj* coupling. This scheme is appropriate for $Ce^{3+}(4f^1; J = \frac{5}{2})$ and $Yb^{3+}(4f^{13}; J = \frac{7}{2})$ because $J = j$ in each case. An extension of this approach to incorporate the effects of crystal-field and Zeeman splittings of the $4f$ states was subsequently carried out by Cornut and Coqblin.[13] Their result takes a particularly simple form in a partial-wave representation

$$\mathcal{H}_{ex}^{(\mathrm{aniso})} = -\sum_{kk'} \sum_{\mathfrak{M}\mathfrak{M}'} \mathcal{J}_{\mathfrak{M}\mathfrak{M}'} C_{k'\mathfrak{M}'}^{\dagger} C_{\mathfrak{M}}^{\dagger} C_{\mathfrak{M}'} C_{k\mathfrak{M}} \quad . \tag{5.12}$$

We have limited Eq. (5.12) to those terms which cause transitions among the local-moment states.

Here $|\mathfrak{M}\rangle$ defines the local-moment eigenstates as before, and $|k\mathfrak{M}\rangle$ the conduction-electron partial waves whose rotational symmetry is identical to that of the localized $4f$ orbitals ($l=3$) in the presence of crystal-field and Zeeman perturbations. The Hamiltonian (5.12) describes a conduction-electron spin and orbital-scattering process in which the angular-momentum index $\mathfrak{M}$ is exchanged with the local-moment. This selection rule contrasts with the $\Delta m_J=0, \pm 1$ selection rules of the isotropic interaction (5.6). Another difference is the dependence of $\mathcal{J}_{\mathfrak{M}\mathfrak{M}'}$ on the states being coupled. Cornut and Coqblin[13] derived an explicit relationship for the exchange parameters

$$\mathcal{J}_{\mathfrak{M}\mathfrak{M}'}=\tfrac{1}{2}|V_{kf}|^2(E_{\mathfrak{M}}^{-1}+E_{\mathfrak{M}'}^{-1}) \ , \tag{5.13}$$

where $V_{kf}$ is the conduction-electron–localized-orbital mixing matrix element (assumed to be independent of $\mathfrak{M}$) and $E_{\mathfrak{M}}(<0)$ the interconfigurational energy ($4f^{13}-4f^{14}$ for $\mathrm{Yb}^{3+}$) relative to the $\mathfrak{M}$th local-moment level. A relationship between $\mathcal{J}_{00}$ and the isotropic exchange constant $\mathcal{J}$ in Eq. (5.6) may be obtained by equating the respective relaxation rates for an isolated $\Gamma_7$ doublet.

$$\begin{aligned}\mathcal{J}_{00}&=(\tfrac{9}{8})^{1/2}(g_J-1)(2J+1)^{1/2}\mathcal{J}\\ &=(\tfrac{3}{7})\mathcal{J} \ \text{ for } J=\tfrac{7}{2} \ .\end{aligned} \tag{5.14}$$

In deriving Eq. (5.14) it is necessary to adjust $\rho^2$ in the anisotropic case by a factor $2/(2J+1)$ to account for the different statistical weights of the $|k\mathfrak{M}\rangle$ states.[13]

For the present purpose the most important consequence of the anisotropic interaction (5.12) is the incoherence between contributions to the second-order matrix element Eq. (5.5) from different virtual transitions. Because of the exchange of the index $\mathfrak{M}$ only a single excited local-moment state $|\mathfrak{M}'\rangle$ can participate in the conduction-electron scattering process $|k'\mathfrak{M}'\rangle \rightarrow |k\mathfrak{M}\rangle$. Although inconvenient for computational purposes, the essential role of orbital exchange scattering in the loss of coherence is easily demonstrated by transforming Eq. (5.12) into a plane-wave representation $|\vec{k}\sigma\rangle$ for the conduction electrons. In this representation contributions from different local-moment transitions are found to be coherent for a given conduction-electron spin-flip transition $\sigma \rightarrow \sigma'$ as in the isotropic case. However, as shown in the Appendix, in the anisotropic case all four possible conduction-electron transitions $\pm\frac{1}{2} \rightarrow \pm\frac{1}{2}$ (i.e., spin-flip as well as non-spin-flip) are effective in driving the nuclear spin-flip transition $m \rightarrow m \pm 1$, with conservation of angular momentum resulting from appropriate changes in the orbital angular momentum of the conduction electrons. On summing Eq. (5.4) over these four distinct processes the interference terms arising from different local-moment transitions are found to vanish.

We proceed by combining Eqs. (5.4), (5.5), and (5.12) to obtain

$$\begin{aligned}T_{\perp}^{-1}&=\frac{1}{9}\frac{\pi}{\hbar}A^2(2J+1)^{-1}\langle\mathcal{J}_{00}^2\rangle\rho^2k_BT\\ &\quad\times\sum_{m\neq 0}R_m^2(|\langle\mathfrak{M}_m|J^+|\mathfrak{M}_0\rangle|^2+|\langle\mathfrak{M}_m|J^-|\mathfrak{M}_0\rangle|^2)\\ &\quad\quad\times[E(\mathfrak{M}_m)-E(\mathfrak{M}_0)]^{-2} \ ,\end{aligned} \tag{5.15}$$

where $R_m \equiv \mathcal{J}_{0m}/\mathcal{J}_{00}$. We observe that the selection rules are determined by $J^{\pm}$ in $\mathcal{H}_{\mathrm{hf}}$ as in the isotropic-exchange theory.

In their analysis of the *Au* $^{170}$Yb ME linewidths Gonzales-Jimenez *et al.*[14] simplified Eq. (5.12) by assuming the $\Gamma_6$ and $\Gamma_8$ levels to be degenerate, and guided by Eq. (5.13) defined three exchange constants $\mathcal{J}_{00}$, $\mathcal{J}_{01}$, and $\mathcal{J}_{11}$, where 0 and 1 denote the $\Gamma_7$ and $\Gamma_8+\Gamma_6$ levels, respectively. We have adopted the same parametrization, thereby ignoring possible field dependences in $\mathcal{J}_{\mathfrak{M}\mathfrak{M}'}$ through Eq. (5.13) as was also done by Bhattacharjee and Coqblin[37] in their analysis of the *Au* $^{171}$Yb high-field ME relaxation rates. With this simplification the $R_m$ in Eq. (5.15) are reduced in number to the single parameter $R_1 \equiv \mathcal{J}_{01}/\mathcal{J}_{00}$.

The results of calculations based on Eq. (5.15), using $\langle\mathcal{J}_{00}^2\rangle\rho^2=(\frac{3}{7})^2\times 0.018$ and treating $R_1$ as an adjustable parameter, are shown in Figs. 12 and 13 for the [001] and [111] field orientations, respectively. (To facilitate comparison with experiment we have reproduced our data in these figures.) The large decrease in the $\Gamma_7$-$\Gamma_8$ fluctuation contribution is immediately apparent on comparing the $R_1=1.0$ curves with the corresponding curves in Figs. 9 and 10. Unfortunately, the reduced sensitivity to the $\Gamma_7$-$\Gamma_8$ exchange-coupling prevents us from establishing the magnitude of the anisotropy constant $R_1$. Although the value $R_1=1.5$ suggested by Gonzales-Jimenez *et al.*[14] would appear to fall outside the error limits of our [001] experimental results, this conclusion is dependent on the assumed value for $\langle\mathcal{J}_{00}^2\rangle\rho^2$. Actually, the Gonzales-Jiminez *et al.* result $\langle\mathcal{J}_{00}^2\rangle\rho^2=0.0035$ (corresponding to $\langle\mathcal{J}^2\rangle\rho^2=0.019$) would shift the theoretical $T_2$ curves toward *shorter* relaxation times by approximately 6% thus increasing the disparity between the $R_1=1.5$ predictions and experiment. On the other hand decreasing $\langle\mathcal{J}_{00}^2\rangle\rho^2$ to its lower bound ($=0.0026$) set by the ESR thermal broadening experiments ($\langle\mathcal{J}^2\rangle\rho^2=0.017\pm0.003$) raises the $R_1=1.5$ curve into the range of our $T_2$ results. Despite the uncertainty regarding the *magnitude* of the anisotropy in the exchange constants it is clear that the anisotropic *form* of the *exchange Hamiltonian* provides an unambiguous explanation for our experimental observations. To be consistent with our results, it follows that any isotropic contribution to the exchange interaction must be relatively small, although not necessarily zero.

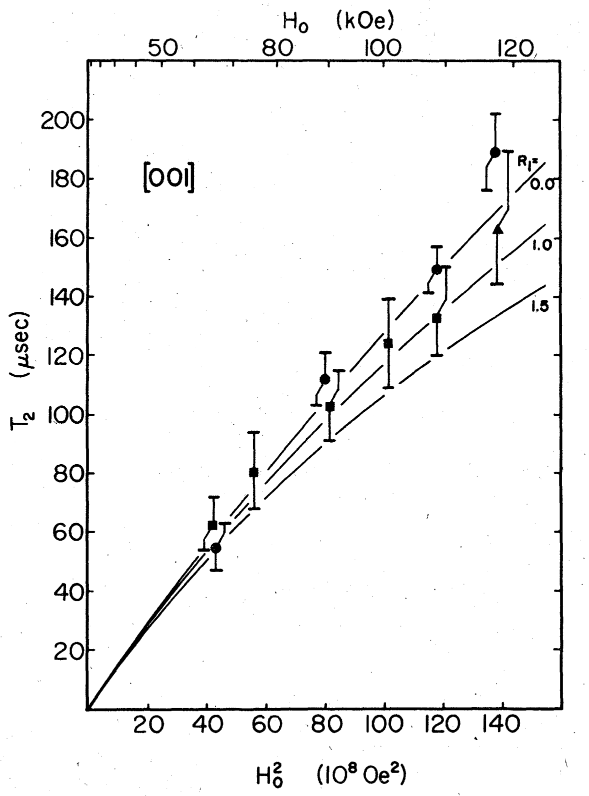

FIG. 12. Comparison of the [001] data in Fig. 9 with theoretical predictions of the anisotropic exchange model for three values of the parameter $R_1 \equiv \mathcal{J}_{01}/\mathcal{J}_{00}$.

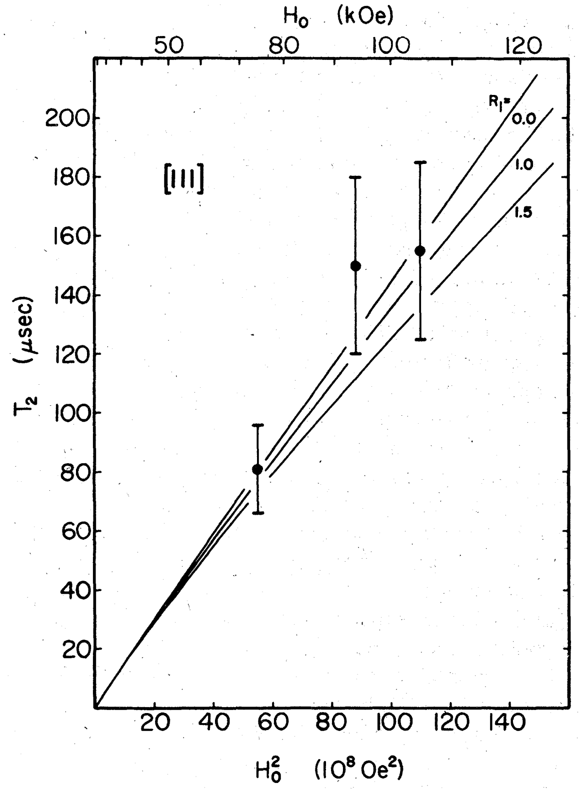

FIG. 13. Comparison of the [111] data in Fig. 10 with theoretical predictions of the anisotropic exchange model for three values of the parameter $R_1 \equiv \mathcal{J}_{01}/\mathcal{J}_{00}$.

## VI. CONCLUSIONS

The present work demonstrates the feasibility of single-crystal transient NMR studies of polarized localized moments in dilute alloys. The information derived from our experiments divides naturally into two kinds. (i) The resonance frequencies probe the static local-moment susceptibility $\chi(0)$; (ii) the transverse nuclear relaxation rates probe the local-moment fluctuation amplitude at $\omega_n$ or, equivalently, the spectral density $\text{Im}\chi^{+-}(\omega_n)/\omega_n$. In contrast, ESR probes $\text{Im}\chi^{+-}(\omega)/\omega$ in the vicinity of the electron-spin-resonance frequency $\omega = \omega_e$ whose thermal broadening measures $(T_2^e)^{-1}$. The ME linewidths, on the other hand, are related to the lifetimes of the local-moment states and thus to $T_1^e$.

The static NMR measurements for the [001] orientation yield values for the *Au* $^{173}$Yb hyperfine constant and crystal-field splitting $\Delta_1$ which are more accurate than previous determinations based on ESR, ME, and susceptibility measurements, as summarized in Table V. The error limits for the NMR-derived hyperfine constant span the entire range permitted by uncertainties in $\Delta_1$ and $K$. (If allowance is made for the small hyperfine anisotropy the error limits for $A$ increase slightly as can be deduced from Fig. 6.) The same consideration applies to the quoted error limits for the crystal-field-parameter splitting $\Delta_1$. The NMR results are unfortunately insensitive to $\Delta_2$ and the exact position of the $\Gamma_6$ level therefore remains uncertain.

The nuclear relaxation rates depend on the magnitude and functional form of the local-moment–conduction-electron exchange interaction. Our results establish unequivocally the dominance of the aniso-

TABLE V. Comparison of experimental hyperfine and crystal-field parameters for *Au* $^{173}$Yb.

| | | $-A/h$ (MHz) | $\Delta_1$ (K) | $\Delta_2$ (K) |
|---|---|---|---|---|
| Present work | | 241.5(1.0) | 83.7(2.5) | |
| Susceptibility | (Ref. 6) | | 80(9) | 83(6) |
| | (Ref. 7) | | 94 | 91 |
| ESR | (Ref. 8) | 247(4) | | |
| ME | (Ref. 9) | 241(7) | | |

tropic exchange form for *Au*Yb. More specifically, the observed ineffectiveness of the excited crystal-field levels in contributing to the high-field $^{173}$Yb relaxation provides strong evidence that all four $\sigma \rightarrow \sigma'$ conduction-electron spin-flip channels participate in a given local-moment transition. The absence of any selection rules on $\Delta\sigma$ can be attributed to orbital terms in the exchange Hamiltonian which assure conservation of total angular momentum. This result is, of course, independent of the magnitude of the anisotropy as expressed by the $\mathfrak{M},\mathfrak{M}'$ dependence of the exchange parameters $\mathcal{J}_{\mathfrak{M}\mathfrak{M}'}$.

As concerns fluctuations between the $\Gamma_7$ doublet levels, our results provide additional support for the values of $\mathcal{J}_{00}$ derived previously from ESR and ME experiments. The agreement with the ESR thermal-broadening measurements[8] is especially noteworthy considering that these experiments probe $\mathrm{Im}\chi^{+-}(\omega)$ at much higher frequencies and in the presence of much weaker magnetic fields than is the case for our NMR experiments.

Regarding the anisotropy parameter $R_1$, only qualitative conclusions can be drawn from the NMR results. As pointed out in Sec. V C the observed field dependence of the $^{173}$Yb relaxation rates suggests a value near unity. A value as large as that obtained by Gonzales-Jimenez *et al.*[14] requires a somewhat smaller value for $\mathcal{J}_{00}$ than assumed by these authors. This disparity, though small, would increase should any *isotropic* terms contribute significantly to the exchange interaction. According to Eq. (5.13) an anisotropy $R_1 = 1.5$ implies $E_0/E_1 = 2$ or, equivalently, a $4f^{13}$-$4f^{14}$ interconfigurational energy comparable in magnitude to the $\Gamma_7$-$\Gamma_8$ crystal-field splitting. Such a value for $E_0$-$E_1$ appears in our judgment surprisingly small. In this connection it is noteworthy that Stöhr[38] was able to account for his high-field ME data with $R_1 \simeq 1.0$. Finally we remark that Stöhr's data combined with the theoretical analysis of Bhattacharjee and Coqblin[37] demonstrate that contributions to the local-moment relaxation rate of third order in the exchange interaction become unimportant for field strengths above ~10 kOe. This result justifies the neglect of higher-order terms in our perturbation calculation.

## ACKNOWLEDGMENTS

We wish to thank W. J. Meyer for his contributions during the preliminary stages of this study. We are also grateful to R. Baughman for growing the single-crystal samples and D. C. Barham for invaluable technical assistance in developing and operating the high-frequency spectrometer. This work was supported by the U. S. DOE.

## APPENDIX

Following Coqblin and Schrieffer,[12] the anisotropic-exchange Hamiltonian (5.12) can be transformed into a plane-wave representation by first noting that the local-moment eigenfunctions for the case of *jj* coupling, are given formally by linear combinations of $J^z = M$ eigenstates

$$|J,\mathfrak{M}\rangle = \sum_{M} \xi_{M\mathfrak{M}} |J,M\rangle \tag{A1}$$

$$= \sum_{M} \xi_{M\mathfrak{M}} (\alpha_M |l, M+\tfrac{1}{2}, \sigma, -\tfrac{1}{2}\rangle + \beta_M |l, M-\tfrac{1}{2}, \sigma, +\tfrac{1}{2}\rangle) \ , \tag{A2}$$

where $\alpha_m$ and $\beta_M$ are Clebsch-Gordan coefficients relating the $|l, \sigma, J, M\rangle$ and $|l, m_l, \sigma, m_\sigma\rangle$ representations. The partial-wave operators are therefore

$$C^{\dagger}_{k\mathfrak{M}} = \sum_{\Omega_{\vec{k}}} \sum_{\sigma} c_{\vec{k}\sigma} \sum_{M} \xi_{M\mathfrak{M}} [\alpha_M Y_l^{M+1/2}(\Omega_{\vec{k}}) \delta_{\sigma,-1/2} + \beta_M Y_l^{M-1/2}(\Omega_{\vec{k}}) \delta_{\sigma,+1/2}] \ , \tag{A3}$$

where $Y_l^{ml}(\Omega_{\vec{k}})$ are the angular-momentum eigenfunctions, and $\Omega_{\vec{k}}$ specifies the orientation of the conduction-electron wave vector with respect to the $z$ axis. We therefore have

$$\mathcal{H}_{\mathrm{ex}}^{\mathrm{aniso}} = - \sum_{\vec{k},\vec{k}'} \sum_{\sigma,\sigma'} \sum_{\mathfrak{M},\mathfrak{M}'} \mathcal{J}_{\mathfrak{M}\mathfrak{M}'}^{\vec{k}\sigma\,\vec{k}'\sigma'} C^{\dagger}_{\vec{k}'\sigma'} C^{\dagger}_{\mathfrak{M}} C_{\mathfrak{M}'} C_{\vec{k}\sigma} \ , \tag{A4}$$

where

$$\mathcal{J}_{\mathfrak{M}\mathfrak{M}'}^{\vec{k}\sigma,\vec{k}'\sigma'} = 4\pi \mathcal{J}_{\mathfrak{M}\mathfrak{M}'} \sum_{M,M'} \xi^{*}_{M,\mathfrak{M}} \xi_{M'\mathfrak{M}'} [\alpha_M Y_l^{M+1/2}(\Omega_{\vec{k}}) \delta_{\sigma,-1/2} + \beta_M Y_l^{M-1/2}(\Omega_{\vec{k}}) \delta_{\sigma,+1/2}]$$

$$\times [\alpha_{M'} Y_l^{M'+1/2}(\Omega_{\vec{k}'})^{*} \delta_{\sigma',-1/2} + \beta_{M'} Y_l^{M'-1/2}(\Omega_{\vec{k}'})^{*} \delta_{\sigma'+1/2}] \ . \tag{A5}$$

We wish to prove that the use of Eq. (A4) in the calculation of the second-order matrix element $H_{if}^{(2)}$ [Eq. (5.5)] leads on summing over $i$, $f$ according to Eq. (5.4) to a cancellation of all interference terms arising from different local-moment transitions. For this purpose we only need to examine the $M' \neq M''$ cross terms arising from Eq. (5.4), the relevant parts of which are

$$\sum_{\Omega_{\vec{k}},\,\Omega_{\vec{k}'}}\ \sum_{\sigma,\sigma'} \mathcal{J}_{\mathfrak{M}\mathfrak{M}'}^{\vec{k}\sigma,\vec{k}'\sigma'}\,\mathcal{J}_{\mathfrak{M}\mathfrak{M}''}^{\vec{k}\sigma,\vec{k}'\sigma'} = (4\pi)^2 \mathcal{J}_{\mathfrak{M}\mathfrak{M}'}\mathcal{J}_{\mathfrak{M}\mathfrak{M}''} \sum_{M,M'} |\xi_{M\mathfrak{M}}|^2 \xi_{M'\mathfrak{M}'}\xi^*_{M'\mathfrak{M}''}(\beta_M^2\beta_{M'}^2+\beta_M^2\alpha_{M'}^2+\alpha_M^2\beta_{M'}^2+\alpha_M^2\alpha_{M'}^2)\,. \quad \text{(A6)}$$

In deriving the right-hand side of Eq. (A6) we made use of the orthonormality property of the spherical harmonics

$$\int d\,\Omega_{\vec{k}} Y_l^m(\Omega_{\vec{k}})\, Y_l^{m'}(\Omega_{\vec{k}})^* = \delta_{m,m'}\ . \quad \text{(A7)}$$

The four terms in the parentheses in Eq. (A6) arise, respectively, from the $\sigma \rightarrow \sigma'$ transitions $+\frac{1}{2} \rightarrow +\frac{1}{2}$, $+\frac{1}{2} \rightarrow -\frac{1}{2}$, $-\frac{1}{2} \rightarrow +\frac{1}{2}$, and $-\frac{1}{2} \rightarrow -\frac{1}{2}$. The sum of these terms is seen to equal 1 and thus to be independent of $M$ and $M'$ because of the normalization relation $\sigma_M^2+\beta_M^2=1$. It follows that Eq. (A6) vanishes identically because of the orthonormality of the local moment eigenstates

$$\sum_{M'} \xi_{M'\mathfrak{M}'}\xi^*_{M'\mathfrak{M}''} = \delta_{\mathfrak{M}',\mathfrak{M}''}\ , \quad \text{(A8)}$$

completing the proof.

---

[1] A. Narath, CRC Crit. Rev. Solid State Sci. 3, 1 (1972).

[2] R. E. Walstedt and W. W. Warren, Jr., Phys. Rev. Lett. 31, 365 (1973).

[3] A. Narath, Phys. Rev. B 13, 3724 (1976).

[4] Preliminary results have been reported by (a) D. M. Follstaedt and A. Narath, Phys. Rev. Lett. 37, 1490 (1976); and (b) D. M. Follstaedt, W. J. Meyer, and A. Narath, *Proceedings of the International Conference on Magnetism '76* (North-Holland, Amsterdam, 1977), p. 507.

[5] A. Benoit, J. Flouquet, and J. Sanchez, Phys. Rev. B 9, 1092 (1974).

[6] G. Williams and L. L. Hirst, Phys Rev. 185, 407 (1969).

[7] A. P. Murani, J. Phys. C 2, S153 (1970).

[8] L. J. Tao, D. Davidov, R. Orbach, and E. P. Chock, Phys. Rev. B 4, 5 (1971).

[9] F. Gonzales-Jimenez and P. Imbert, Solid State Commun. 11, 861 (1972).

[10] F. Gonzales-Jimenez and P. Imbert, Solid State Commun. 13, 85 (1973).

[11] G. K. Shenoy, J. Stöhr, W. Wagner, G. M. Kalvius, and B. D. Dunlap, Solid State Commun. 15, 1485 (1974).

[12] B. Coqblin and J. R. Schrieffer, Phys. Rev. 185, 847 (1969).

[13] B. Cornut and B. Coqblin, Phys. Rev. B 5, 4541 (1972).

[14] F. Gonzales-Jimenez, B. Cornut, and B. Coqblin, Phys. Rev. B 11, 4674 (1975).

[15] N. L. Huang Liu, K. J. Ling and R. Orbach, Phys. Rev. B 14, 4087 (1976).

[16] W. Fert, in Ref. 4(b), p. 491.

[17] M. E. Sjostrand and G. Seidel, Phys. Rev. B 11, 3292 (1975).

[18] A. Narath and D. C. Barham, Rev. Sci. Instrum. 45, 100 (1974).

[19] N. Sano, S. Kobayashi, and J. Itoh, Prog. Theor. Phys. Suppl. 46, 84 (1970).

[20] T. S. Stakelon and D. M. Follstaedt, Rev. Sci. Instrum. 49, 45 (1978).

[21] A. Abragam and B. Bleaney, *Electron Paramagnetic Resonance of Transition Ions* (Clarendon, Oxford, 1970), p. 221.

[22] D. C. Barham (unpublished).

[23] S. Ofer, I. Nowik, and S. G. Cohen, in *Chemical Applications of Mössbauer Spectroscopy,* edited by V. I. Goldanskii and R. H. Herber (Academic, New York, 1968), p. 428.

[24] A. C. Gossard, V. Jaccarino, and J. H. Wernick, Phys. Rev. 133, A881 (1964).

[25] A. Narath, Phys. Rev. 179, 359 (1969).

[26] A. Narath and A. T. Fromhold, Jr., Phys. Rev. 139, A794 (1965).

[27] A. M. Clogston, V. Jaccarino, and Y. Yafet, Phys. Rev. 134, A650 (1964).

[28] A. Abragam and B. Bleaney, in Ref. 21, p. 149.

[29] K. R. Lea, M. J. M. Leask, and W. P. Wolf, J. Phys. Chem. Solids 23, 1381 (1962).

[30] S. Geschwind, in *Hyperfine Interactions,* edited by A. J. Freeman and R. B. Frankel (Academic, New York, 1967), p. 251.

[31] Y. Yafet and V. Jaccarino, Phys. Rev. 133, A1630 (1964).

[32] R. E. Walstedt, Phys. Rev. Lett. 19, 146 (1967); 19, 816 (1967).

[33] A. Narath and D. Follstaedt (unpublished).

[34] R. E. Walstedt and A. Narath, Phys. Rev. B 6, 4118 (1972).

[35] A. Narath, Phys. Scripta 11, 237 (1975).

[36] L. L. Hirst, G. Williams, I. Griffiths, and B. R. Coles, J. Appl. Phys. 39, 844 (1968).

[37] A. K. Bhattacharjee and B. Coqblin, Solid State Commun. 18, 1587 (1976).

[38] J. Stöhr, Phys. Rev. B 11, 3559 (1975).